

## Laboratory Wave and Stress Measurements Quantify the Aerodynamic Sheltering in Extreme Winds

Peisen Tan<sup>1</sup> , Andrew W. Smith<sup>2</sup> , Milan Curcic<sup>1</sup> , and Brian K. Haus<sup>1</sup> 

<sup>1</sup>Rosenstiel School of Marine, Atmospheric and Earth Science, University of Miami, Miami, FL, USA, <sup>2</sup>Imperial College London, London, UK

### Key Points:

- Sheltering coefficient is not constant as was previously assumed
- Sheltering coefficient is highly variable and depends on both the wind speed and the wave state
- The location of the steepest wind waves on the long-wave phase illustrates the aerodynamic sheltering

### Supporting Information:

Supporting Information may be found in the online version of this article.

### Correspondence to:

P. Tan,  
[pxt254@miami.edu](mailto:pxt254@miami.edu)

### Citation:

Tan, P., Smith, A. W., Curcic, M., & Haus, B. K. (2023). Laboratory wave and stress measurements quantify the aerodynamic sheltering in extreme winds. *Journal of Geophysical Research: Oceans*, 128, e2022JC019505. <https://doi.org/10.1029/2022JC019505>

Received 20 NOV 2022

Accepted 20 MAR 2023

### Author Contributions:

**Conceptualization:** Brian K. Haus

**Data curation:** Peisen Tan

**Formal analysis:** Peisen Tan, Milan Curcic

**Funding acquisition:** Milan Curcic, Brian K. Haus

**Investigation:** Peisen Tan, Andrew W. Smith, Milan Curcic

**Methodology:** Peisen Tan, Milan Curcic

**Project Administration:** Brian K. Haus

**Supervision:** Andrew W. Smith, Milan Curcic, Brian K. Haus

**Validation:** Andrew W. Smith, Milan Curcic

**Visualization:** Peisen Tan

**Writing – original draft:** Peisen Tan

**Writing – review & editing:** Peisen Tan, Andrew W. Smith, Milan Curcic, Brian K. Haus

© 2023. The Authors.

This is an open access article under the terms of the [Creative Commons Attribution License](https://creativecommons.org/licenses/by/4.0/), which permits use, distribution and reproduction in any medium, provided the original work is properly cited.

**Abstract** In strong winds, air flow detaches from the ocean surface in the lee of wave crests and creates a low-pressure zone on the wave's leeward face. The pressure difference between the wave's rear and front face modulates the momentum input from wind to waves. Numerical wave models parameterize this effect using a so-called sheltering coefficient. However, its value and dependence on wind speed are not well understood, particularly with background swell waves. To bridge this gap, we conducted laboratory experiments with winds up to Category 4 hurricane force blown over various mechanically generated wave conditions (pure wind sea, mixed waves with directional spreading, and monochromatic unidirectional waves) and measured the wind, waves, and stress at a sufficient frequency to resolve wind-wave variability over the long-wave phase. We analyze the results in the context of Jeffreys's sheltering theory and find two regimes: (a) from low-to-moderate wind forcing ( $10 \text{ m s}^{-1} < U_{10} < 33 \text{ m s}^{-1}$ ), the aerodynamic sheltering increases with wind speed, consistent with previous studies; (b) in hurricane conditions ( $U_{10} > 33 \text{ m s}^{-1}$ ), the aerodynamic sheltering decreases with wind at a rate depending on wave state. Further, we isolate the short wind waves from the longer paddle waves and find that the aerodynamic sheltering by longer waves leads to a phase-dependent variability of the short wind-waves' local steepness, which is evidenced by the sheltering coefficient's value derived from wind and wave measurements. Our results emphasize the need for further measurements of aerodynamic sheltering and improving its representation in models.

**Plain Language Summary** When the wind blows over the water surface, the leeward side of the wave is sheltered by the windward side. The sheltering has historically been quantified using an empirical parameter. Our research shows that this empirical parameter is not constant as previous studies have often assumed. Instead, its value depends on the wind speed and wave form. We also show that the sheltering is evidenced by the location of the steepest wind waves on the long wave, which we also see in the camera images of the wave surface.

## 1. Introduction

Wave growth is governed to first-order by momentum flux from the wind, which in turn feeds back to affect the exchange of momentum from wind to the ocean surface and subsurface (Grare et al., 2013). Under wind forcing, smaller waves on the leeward side of larger waves are sheltered from the wind. Better understanding and quantifying the role of sheltering on wave growth under wind forcing remains elusive. The sensitivity of sheltering to different background waves, especially under extreme wind forcing, is also not well understood. This is important because tropical cyclones are known to have complex wind-wave states in different quadrants of the storm (Wright et al., 2001).

One of the most popular theories that incorporate sheltering is the Jeffreys's sheltering (JS) hypothesis (Jeffreys, 1924, 1925). The JS hypothesis is based on the geometric form of the wavy surface: when wind blows over the water surface, the waves induce a flow separation on the leeward side of the wave and the air flow detaches from the wave surface and creates a low-pressure area. Thus, the lee of wave is sheltered by the windward side of the wave.

Two wave growth theories alternative to JS were proposed by Phillips (1957) and Miles (1959). Phillips (1957) argued that the initial wave growth relies on a resonance between surface waves and the pressure fluctuations in the wind. The wind has a turbulent component—composed of an ensemble of eddies—as it blows over the water surface. The pressure disturbances associated with those eddies generate ripples on the water surface. As waves grow higher, the resonance plays a lesser role in wave growth. Thus, Phillips theory is relevant only for

initial wave growth on a calm water surface (Li & Shen, 2022). Miles theory, on the other hand, assumed that the transfer of energy occurs at the critical height where the wind speed equals the phase speed ( $C_p$ ) of the waves. The transfer of energy from wind to waves is proportional to the curvature of the mean velocity profile at the critical height. Miles theory is thus more applicable for more developed waves than Philips theory. Further, similar to the JS hypothesis, Miles theory also considers the wind-wave coupling and the momentum flux in the context of a structural change of waves. However, the supporting physical mechanisms behind Miles theory and the JS hypothesis are different.

Both the Miles and the JS theories have been studied in laboratory and numerical studies to test their validity. Donelan et al. (2006) found experimentally that the air-flow separation occurs when the acceleration needed to keep the air flow attached to the surface downstream of the crest (referred to as centripetal acceleration) exceeds the downward vertical acceleration of the wave-induced flow at the crest, thus leading to sheltering. Savelyev et al. (2011) suggested that the sheltering mechanism from air-flow separation over the water surface supported by JS hypothesis becomes dominant compared to the nonseparated mechanism and enhances the wind-wave momentum flux for wave steepness  $ak$  (defined as wave amplitude  $a$  times wavenumber  $k$ ) greater than 0.19. Using Particle Image Velocimetry (PIV) in a large wind-wave-current tank, Buckley and Veron (2016) found that the air flow over young waves (wave age  $C_p/u_* < 3.7$ , where  $u_*$  is the friction velocity) separates from the water surface downwind of the wave crest and a large sheltering effect was observed past the wave crest. Further, Buckley and Veron (2019) confirmed the drastic modification of wind stress by waves due to sheltering. In their research, for the wind forcing  $U_{10}$  (the wind speed at 10 m height above the water surface) of 9.41 and 16.63 m s<sup>-1</sup>, the wave-induced stress was positive above both windward and leeward faces of the waves and negative elsewhere.

The wave growth theories have also been extensively studied from a numerical point of view. Touboul et al. (2008) found that the JS theory is more accurate than the Miles theory by simulating freak wave growth under wind forcing, based on the Nonlinear Schrödinger Equation (NSE). Montalvo et al. (2013) extended the Miles theory to finite depth and derived a wind-forced finite-depth NSE. They showed analytically that the sheltering mechanism in JS hypothesis is dominant compared to the Miles theory during the process of wave growth in young waves ( $C_p/u_* < 7$ ) when they are steep enough to induce sheltering. Using Large Eddy Simulations (LES), Yang et al. (2013) demonstrated that the sheltering in the troughs due to the flow separation at the crests agrees with the calculated growth rates from many experiments. Husain et al. (2022) used LES and phase-averaged turbulent kinetic energy (TKE), vorticity, wave dissipation, and wind stress on young waves ( $C_p/u_* < 1.4$ ). Their results show a clear air-flow separation on the leeward face of the long waves, forming a pressure “dead zone” and the TKE gradually increasing from near-zero to a maximum on the windward face of the wave in front. Further, due to the positive-definite  $(U_*/C_p)^2$  in the wave growth parameterization based on the Miles theory, it cannot resolve negative flux that occurs in calm wind over swell. Miles theory can thus only be applied to young wind sea where waves are slower than and aligned with the wind (Riley et al., 1982). In contrast, the JS hypothesis is applicable in swell and wind sea alike because it permits the momentum flux to be of either sign.

To quantify sheltering in a numerical wave model, Donelan et al. (2012) used an empirical sheltering coefficient  $A$  in the parameterization of JS. In their model, the coefficient  $A$  is defined in the range [0, 1] and corresponds to the unit area of the water surface that is exposed to the wind forcing.  $A = 1$  implies no sheltering (wind follows the wavy surface) and  $A = 0$  implies complete sheltering (wind is completely detached from the wavy surface). Smaller  $A$  thus imply smaller wind input to the waves. Being a key parameter, the choice of the value of  $A$  can greatly affect the resulting wave growth rates and thus the accuracy of the model altogether. By validating the model against in situ wind and wave measurements in both tropical and extratropical storms, Donelan et al. (2012) iteratively determined the value of  $A$  to be 0.11, 0.10, and 0.01 in the cases of wind following waves, wind opposing waves, and waves outrunning wind (swell) conditions, respectively. While some previous studies (Donelan, 1999; Donelan & Pierson, 1987; Donelan et al., 2012) assumed  $A$  a constant, several experimental studies (Grare, 2009; Grare et al., 2013; Mastenbroek et al., 1996; Peirson & Garcia, 2008) found  $A$  in the range [0.1, 0.5], and its value decreasing with increasing wave steepness. There is thus mounting evidence that steeper waves lead to more pronounced aerodynamic sheltering.

Although sheltering has been studied under different wind-sea conditions (Buckley & Veron, 2019; Grare et al., 2013; Savelyev et al., 2011), the exact value of the sheltering coefficient  $A$  remains unknown in strong winds ( $U_{10} > 30$  m s<sup>-1</sup>). Further, the dependence of  $A$  on the geometric form of background waves remains

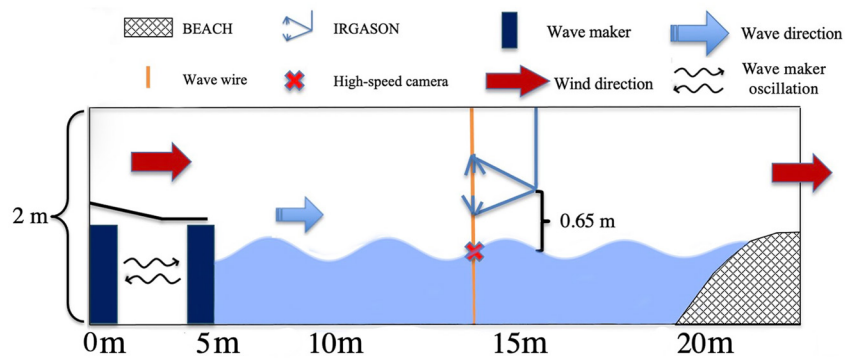


**Figure 1.** Diagram of the experimental setup in the SUSTAIN Laboratory. The vertical and horizontal dimensions are not to scale. The wind-wave tank consists a single-pass air system from the fan on the left where the wind is generated to the beach at the end of the tank on the right where the air exits the tank. A cross-tank offset of 1 m exists between the wave wire and the IRGASON sonic anemometer.

unknown. Due to the lack of systematic research on the value of  $A$  in the JS theory, researchers have argued that the JS hypothesis does not accurately depict the wave growth due to wind (Hristov, 2018; Stewart, 1967). Therefore, a thorough study of the sheltering coefficient—particularly in extreme wind conditions—is vital for better understanding aerodynamic sheltering and the improvement of numerical wave models as an essential component of coupled atmosphere–wave–ocean models for hurricane research and prediction.

To fill this gap, we subjected multiple mechanically generated initial waves to strong winds (from 10.9 to 65.9 m s<sup>−1</sup>, up to Category 4 hurricane intensity) in a series of laboratory experiments. From in situ and high-frequency measurements of water elevation and air turbulence, we computed the sheltering coefficient to quantify the sheltering in such wind-wave conditions. We characterized sheltering in terms of wave statistical properties with support from visible-camera imagery of the wavy surface. Our study shows the behavior of the sheltering coefficient in strong winds under different wave forms and guides the future development of wind input parameterizations in the next generation wave models.

## 2. Methods

### 2.1. Jeffreys's Sheltering Hypothesis

Donelan et al. (2012) parameterized the wave energy input from wind  $S_{in}$  using the directional wave spectrum in Equation 1 of their paper. We assume conditions with no background current, waves aligned with wind direction, and omni-directionality of the wave field. Integrating their equation over directional space and casting it in the frequency domain:

$$S_{in}(f) = A \frac{\rho_a}{\rho_w} \left( \frac{U_{\lambda/2}}{C_p} - 1 \right) \left| \frac{U_{\lambda/2}}{C_p} - 1 \right| \omega E(f) \quad (1)$$

where  $\rho_a$  and  $\rho_w$  are air and water density,  $f$  is wave frequency,  $E(f)$  is the spectral wave energy density in frequency space,  $\omega$  is the wave angular frequency,  $C_p$  is the wave phase speed, and  $A$  is the sheltering coefficient. Equation 1 states that the wind input (the rate of wave variance spectrum change due to wind forcing) is proportional to the sheltering coefficient, the air to water density ratio, the sign-preserving wave-relative wind speed, and the wave spectrum. In this paper, we conduct a systematic research on the variability of  $A$  under different wind forcing and wave conditions. The experimental setup is described in the following subsection.

### 2.2. Laboratory Measurements

Our research was conducted at the SURge Structure Atmosphere Interaction (SUSTAIN) Facility at the University of Miami's Rosenstiel School of Marine, Atmospheric and Earth Science. A schematic of the facility is shown in Figure 1. The laboratory contains a wind tunnel built over a wave tank with a 23-m long, 6-m wide, and 2-m tall working section. The wave tank is equipped with a programmable, oscillating, mechanical wave-maker

**Table 1**  
*Experimental Parameters Used in the Research*

Experiment	Fan frequency (Hz)	Paddle waves
WO	10–50	None
J10	10–50	JONSWAP, $H_{sig} = 10$ cm, $f_p = 1$ Hz
M7.5	10–50	Monochromatic, $a = 7.5$ cm, $f_p = 1$ Hz

consisting of 12 paddles. The wave-maker can generate monochromatic or broad-banded waves with or without directional spreading. A porous parabolic beach dissipates incoming wave energy with minimum reflection. The wind tunnel is capable of generating free-stream velocities exceeding Category 5 hurricane intensity ( $U_{10} > 70$  m s<sup>-1</sup>).

Wind velocity was measured using a Campbell Scientific 3-day sonic anemometer and infrared gas analyzer (IRGASON). The anemometer was placed at 9 m down-fetch from the wind inlet at 0.65 m height above the water surface. Its sampling frequency is 20 Hz. IRGASON's precision for

horizontal and vertical velocities is 1 and 0.5 mm s<sup>-1</sup>, respectively. The instantaneous water surface elevation was obtained by a capacitance wave wire gauge at a sampling frequency of 20 Hz. The wave wire was placed at the same fetch as the IRGASON but 2 m away from it in the negative cross-tank direction (to the right when facing the beach). At the same fetch and outside of the tank, a camera was mounted and pointed in the cross-tank direction. The camera was set to capture 20 frames per second and adjusted to focus on the air–water interface nearest to the lens. The image size is 1,000 × 1,000 pixels covering an area of 82.8 cm × 82.8 cm. One pixel thus corresponds to 0.828 mm. This provides a visualization of the air–water interface that coincides with the wave and wind measurements and allows for further analysis and verification of the results.

The wind generator operated at frequencies ranging from 10 to 50 Hz with 5 Hz intervals. Each fan frequency, and thus each wind speed, was maintained for 10 min before transitioning to the next wind condition. The ramping up of wind from one steady-state condition to another takes approximately 30 s, and we excluded it from the analysis.

Three wind-wave conditions were tested: (a) pure wind-sea conditions without paddle waves, referred to as WO (Wind Only) in this paper; (b) initially short-crested JONSWAP (Hasselmann et al., 1973) spectrum of waves at peak frequency  $f_p$  of 1 Hz, significant wave height ( $H_{sig}$ ) of 10 cm, and directional spreading with a  $\cos^2$  shape (referred to as J10 in this paper); and (c) monochromatic waves with 1-Hz frequency (wave length of  $\lambda \approx 0.5$  m) and amplitude  $a = 7.5$  cm (referred as M7.5 in this paper). The purpose of the WO experiment is to provide pure wind-sea conditions that are not sheltered by any long waves. Thus, WO serves as a control experiment against which J10 and M7.5 will be evaluated. The J10 experiment introduces broad-banded background waves that aim to mimic the realistic wave state that can be found in the field. J10 allows us to relate our sheltering results to the real ocean. Finally, the M7.5 experiment introduces steep, monochromatic, background waves that enable phase-dependent analysis, which is necessary for better understanding of the sheltering process. The experimental parameters are shown in Table 1.

The expression for the JONSWAP wave spectrum (Hasselmann et al., 1973) with directional spreading is

$$S(f) = \frac{\alpha g^2}{(2\pi)^4 f^5} \exp \left[ -\frac{5}{4} \left( \frac{f}{f_p} \right)^{-4} \right] \Gamma^r \cos^N(\theta) \quad (2)$$

wherein

$$r = \exp \left[ -\frac{(f - f_p)^2}{2\sigma^2 f_p^2} \right] \quad (3)$$

and  $\alpha$  is the Philips constant determined by the magnitude of the total wave energy.  $\Gamma$  is the peak enhancement factor and is equal to 3.3 in JONSWAP spectrum waves.  $\sigma$  has the value of 0.07 and 0.09 for waves longer and shorter than the peak, respectively.  $\theta$  is the wave spreading angle and  $N$  is the spreading factor with the value of 2 in this study.

The stationary water level  $h$  was set to 0.8 m to allow all waves in the J10 and M7.5 experiments to be deepwater waves ( $h/\lambda > 1/2$ ). However, the characteristics of J10 and M7.5 waves are different. The JONSWAP waves are broad banded and mimic a realistic, random wave field that is similar to that in the open ocean. On the other side, M7.5 waves are monochromatic, unidirectional, sine-like waves. Though such waves are not comparable to those found in the open ocean, they are useful for studying aerodynamic sheltering because they allow clean separation of wind sea and swell and phase-resolved spectral analysis of shortwaves.

After imposing the wind forcing, the water surface features a combination of wind-sea and mechanical waves. We calculated the mean wave steepness parameter  $ak$  following Grare et al. (2013) to characterize the waves consistently across the three experiments. First, we calculate the mean wave frequency  $\bar{f}$  using:

$$\bar{f} = \frac{m_1}{m_0} \quad (4)$$

where  $m_0$  and  $m_1$  are the zeroth and first moments of the wave energy spectrum  $F(f)$ , respectively. The general expression for the  $n$ th spectral moment is

$$m_n = \int_{f_{\min}}^{f_{\max}} f^n F(f) df \quad (5)$$

Given the sampling frequency of the wave wire we use,  $f_{\min} = 0$  Hz and  $f_{\max} = 10$  Hz (Nyquist frequency). Then, we calculate the mean wave height  $\bar{H}$  as

$$\bar{H} = 0.886 H_{rms} = 0.886 \sqrt{m_0} \quad (6)$$

where  $H_{rms}$  is the root mean square wave height. Then, we derive the mean wave number  $\bar{k}$  from  $\bar{f}$  using linear dispersion relation. The mean wave steepness,  $ak$ , is then defined as

$$ak = \frac{\bar{H}}{2} \bar{k} \quad (7)$$

These parameters will be used in the analysis of the results later in the paper.

### 2.3. Wind Stress

We derive the eddy-covariance wind stress following for example, Tennekes and Lumley (1972) and Edson et al. (1998):

$$\tau = \rho_a \sqrt{\left(-\overline{u'w'}\right)^2 + \left(-\overline{v'w'}\right)^2} \quad (8)$$

where  $u'$ ,  $v'$ , and  $w'$  are downwind, cross-wind, and upward perturbation velocities, respectively. As the stress is not constant but linearly decreases with height inside of the tank, the measured values must be extrapolated to the mean water level ( $z = 0$ ) before they can be compared with measurements from the field. This approach is common to laboratory measurements of stress in an enclosed tank (Curcic & Haus, 2020; Donelan & Plant, 2009; Donelan et al., 2004; Uz et al., 2002). To extrapolate the measured stress to the surface, we relate the vertical stress gradient with the horizontal pressure gradient. The stress was measured at heights from 0.1 to 0.6 m using a TSI IFA-300 constant temperature hot-film anemometer and related to the horizontal gradient of air pressure in a wide range of wind speeds, providing a robust linear fit. We provide the details of this procedure in Supporting Information S1. Hereon, all our wind stress estimates are in reference to the mean water surface.

Then, we obtained the friction velocity  $u^*$  at the surface using:

$$u_* = \sqrt{\frac{\tau_s}{\rho_a}} \quad (9)$$

where  $\tau_s$  is the wind stress extrapolated to the surface.

The mean wind speed  $U_z$  for each fan setting was scaled from the measurement height to the standard meteorological 10-m height assuming the logarithmic profile and neutral thermodynamic conditions:

$$U_{10} = U_z + \frac{u_*}{\kappa} \ln\left(\frac{10}{z}\right) \quad (10)$$

where  $\kappa$  is the Von Kármán constant (0.41) and  $z$  is the measurement height (0.65 m). Measured and scaled wind speeds for each experiment and fan setting are shown in Table 2.

The total wind stress consists of two components: the form stress  $\tau_f$  caused by pressure difference between the windward and leeward sides of the wave and the viscous (skin) stress  $\tau_v$  caused by the drag in the viscous sublayer



**Table 2**  
Fan Frequency and Measured and Scaled Mean Wind Speeds From All Experiments

Fan frequency (Hz)	WO	WO	J10	J10	M7.5	M7.5
	$U_z$ (m s <sup>-1</sup> )	$U_{10}$ (m s <sup>-1</sup> )	$U_z$ (m s <sup>-1</sup> )	$U_{10}$ (m s <sup>-1</sup> )	$U_z$ (m s <sup>-1</sup> )	$U_{10}$ (m s <sup>-1</sup> )
10	7.5	10.9	7.4	10.9	8.0	11.4
15	11.5	16.8	11.7	16.9	11.9	16.9
20	15.4	23.1	15.8	23.3	15.7	23.0
25	19.5	30.0	19.9	30.1	19.7	29.5
30	23.5	37.2	24.3	37.6	23.4	36.1
35	27.2	44.3	28.1	44.8	28.2	44.2
40	31.2	51.5	31.6	51.6	32.8	51.8
45	35.2	58.8	35.5	59.0	37.0	59.9
50	39.1	65.9	38.6	66.1	39.7	66.4

(Donelan et al., 2012; Jones & Toba, 2001; Makin et al., 1995; Monin & Yaglom, 1971). As the aerodynamic sheltering is specifically a consequence of the wave form,  $\tau_v$  must be subtracted from the measured stress such that

$$\tau_f = \tau - \tau_v = \rho_a \sqrt{\left(-\overline{u'w'}\right)^2 + \left(-\overline{v'w'}\right)^2} - \tau_v \quad (11)$$

To obtain  $\tau_v$ , we assume the smooth law of wall with a pure laminar flow immediately adjacent to the water surface where (Donelan et al., 2012; Jones & Toba, 2001)

$$U(z) = \frac{u_{*v}}{\kappa} \ln \frac{z}{z_{0v}} \quad (12)$$

where  $u_{*v}$  and  $z_{0v}$  are the viscous friction velocity and roughness lengths, respectively, and are related through the viscous Reynolds number and the kinematic viscosity  $\nu$ :

$$Re = \frac{z_{0v} u_{*v}}{\nu} \quad (13)$$

Jones and Toba (2001) and Donelan et al. (2012) assumed  $Re = 0.11$  for the near-surface laminar air flow. Combining Equations 11–13 yields  $u_{*v}$ ,  $\tau_v$ , and finally  $\tau_f$ .

## 2.4. Sheltering Coefficient

After obtaining  $\tau_f$ , the wind input source function  $S_{in}$  can be linked with  $\tau_f$  following Donelan et al. (2012):

$$\tau_f = \rho_w g \int_{f_{min}}^{f_{max}} \frac{S_{in}(f)}{C_p} df \quad (14)$$

By combining Equations 1 and 14 and assuming the sheltering coefficient is a constant across all wave frequencies, it can be calculated as

$$A = \frac{\tau_f}{\rho_a g \int_{f_{min}}^{f_{max}} \left( \frac{U_{\lambda/2}}{C_p} - 1 \right) \left| \frac{U_{\lambda/2}}{C_p} - 1 \right| k F(f) df} = \frac{\tau_f}{D} \quad (15)$$

Equation 15 states that the sheltering coefficient can be expressed as the ratio of the form stress and the unscaled integral of the wind input into each spectral wave component, defined as  $D$  hereafter (the denominator in Equation 15).  $D$  is largely determined by the squared wave-relative wind speed at the spectral peak. Larger form stress thus leads to larger  $A$  (less sheltering), and larger wave-relative wind speed over high-energy waves leads to smaller  $A$  (more sheltering).

The integration in the denominator makes the expression of  $A$  in Equation 15 frequency independent, so this approach may be inappropriate because aerodynamic sheltering is likely to vary at different wave scales. Thus, in this study, we extend the sheltering coefficient from a uniform parameter  $A$  across wave-frequency spectrum into a frequency-dependent parameter. To achieve this, we compute the velocity cospectrum  $S_{uw}(f)$  and the frequency-dependent wind stress  $\tau(f)$  (Drennan et al., 1999):

$$\tau(f) = -\rho_a S_{uw}(f) \quad (16)$$

An integration of  $\tau(f)$  over  $f$  will yield to  $\tau$  from Equation 8 theoretically. Due to the geometrical nature of sheltering, we assume that the sheltering effect on a particular wave comes from all the waves longer than itself (lower in frequency). Thus, for every specific frequency  $f$ , we integrate the denominator  $D(f)$  over the frequencies that are lower than  $f$ . The frequency-dependent sheltering coefficient  $A(f)$  is then:

$$A(f) = -\frac{\rho_a S_{uw}(f)}{\int_{f_{min}}^f D(f') df'} \quad (17)$$

In this form, the sheltering coefficient is frequency dependent. More energy in the longer waves leads to a smaller  $A(f)$  and larger sheltering for that frequency. Conversely, if the frequency-dependent stress  $-\rho_a S_{uw}(f)$  is larger at a specific frequency, more energy is transferred from wind to waves in that frequency, thus leading to larger  $A(f)$  and smaller sheltering.

## 2.5. Local Steepness

Flow separation, which leads to sheltering, is closely related to wave steepness (Husain et al., 2019). As wave breaking plays a crucial role in the wave steepness variability under wind forcing, studying wave properties that are related to wave breaking will help us understand the variability of sheltering as well. Liu and Babanin (2004) introduced a method to calculate a wave's local steepness based on wavelet transforms. Their method was shown to be accurate in predicting wave growth and breaking by the verification of visual observation of wave breaking events on Lake George and in the Black Sea.

Following Liu and Babanin (2004), we perform a Hilbert Transform on water surface elevation  $\eta_i$  to obtain the local amplitude  $a_i$ :

$$a_i = \mathcal{H}(\eta_i) \quad (18)$$

Subscript  $i$  represents data at a local time point  $t_i$ . Then, a continuous wavelet transform based on the Morlet function was performed on the water surface elevation  $\eta_i$  to obtain the wavelet spectrum  $W(\omega, t)$ . The local phase  $p$  is then obtained from  $W(\omega, t)$ :

$$\phi(\omega, t_i) = \arctan\left(\frac{\Im[W(\omega, t_i)]}{\Re[W(\omega, t_i)]}\right) \quad (19)$$

$\Im[W(\omega, t)]$  and  $\Re[W(\omega, t)]$  are the imaginary and real parts of  $W(\omega, t)$ , respectively. The local characteristic amplitude  $A_i$  is defined as

$$A_i = a_i \cos(\phi_i) \quad (20)$$

and finally the local steepness  $\gamma$  is defined as

$$\gamma_i = A_i \omega_p^2 / g \quad (21)$$

$\omega_p$  is the angular frequency where the energy peak from wavelet spectrum is observed. In this study, we use these properties to investigate the local steepness  $\gamma$ 's variability with wind speed and to relate it to aerodynamic sheltering.

## 2.6. Conditional Phase Average

When shortwaves are sheltered by longer waves, the longer waves modulate the shortwave growth by reducing the wind input. Due to the shape of the wave form, shortwaves may "experience" sheltering differently depending on the phase of the long waves (Donelan et al., 2010; Laxague et al., 2017). The windward face of the long wave receives more wind input than the leeward face. To discuss the modulation of shorter waves by longer waves at different wave phases, Donelan et al. (2006) applied a Hilbert Transform to the mechanically generated long-wave elevation. Based on the phase record from the Hilbert Transform on the long waves, they conditionally sampled and averaged the shortwave properties in select long-wave phase bins. Later, Donelan et al. (2010) discussed the long-wave modulation on the growth of shortwaves generated by winds blown over the surface using conditional phase-averaging on the local wind-sea spectrum based on a wavelet transform. This method successfully revealed the sheltering from different phases of the long wave. Donelan et al. (2010) focused on low-to-moderate winds ( $U_{10} < 15 \text{ m s}^{-1}$ ) due to the limitation of their laboratory. Therefore, the modulation of shortwaves by longer waves in strong winds remains unknown.

Although ocean waves do not exhibit monochromatic behavior but rather are composed of a broadband spectrum, the harmonic form and idealized smoothness of the former aid our ability to isolate and study sheltering. Thus, in our study and following Donelan et al. (2010), we first apply the band-pass filter in the 0.8–1.2 Hz band on the elevation signal of M7.5 to extract the long-wave signal. Then, we use a high-pass filter in the 2.1–2.9 Hz band

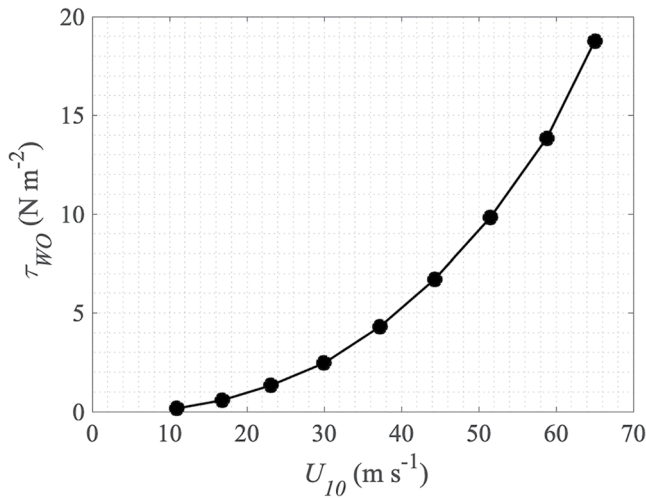


**Figure 2.** Eddy-covariance wind stress from IRGASON in the wind-only experiment, as function of 10-m wind speed.

and 31 m s<sup>-1</sup>, respectively.  $\tau_{J10}$  becomes marginally higher than  $\tau_{WO}$  in the  $U_{10}$  range from 31 to 59 m s<sup>-1</sup>, by up to 2%. However,  $\tau_{M7.5}$  is higher than  $\tau_{WO}$ . In both experiments, the relative stress difference peaks at  $U_{10} = 37$  m s<sup>-1</sup>. In summary, mechanically generated background waves overall cause a wind stress increase in stress except in low-to-moderate winds. This increase is more pronounced in steep monochromatic waves (11% maximum increase) than in broad-banded JONSWAP waves (2% maximum increase). This relative difference is important to establish before we proceed to evaluate the sheltering coefficient for each wind and wave condition in Section 3.4.

### 3.2. Separating the Form and Viscous Stresses

After obtaining  $\tau$  via eddy covariance, the separation of  $\tau_f$  and  $\tau_v$  described in Section 2.3 was performed and the ratio of the form stress  $\tau_f$  fraction of the total stress  $\tau$  is plotted against  $U_{10}$  for all three experiments (Figure 4). We also compare our measurements with the numerical results from Donelan et al. (2012) for reference. Overall,  $\tau_f$  constitutes approximately 60% of total stress at  $U_{10} \approx 10$  m s<sup>-1</sup> and increases with wind speed to approximately 90% of the total stress at  $U_{10} \approx 65$  m s<sup>-1</sup>.

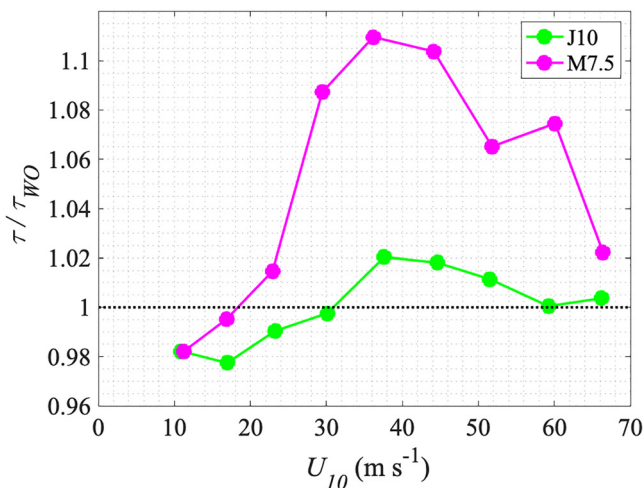


**Figure 3.** Eddy-covariance wind stress from IRGASON, normalized by  $\tau_{WO}$ , from the J10 (green) and M7.5 experiments, as a function of 10-m wind speed from the Wind Only (WO) experiment.

to extract the short wind waves. Finally, we perform the method by Liu and Babanin (2004) to get the local wavelet spectrum  $W_s$  and local steepness  $\gamma_s$  of short wind-wave signal. Finally, we used 10° bins and phase average  $W_s$  and  $\gamma_s$  over the long-wave phases to quantify the variability of shortwave properties depending on the long-wave phase.

## 3. Results

### 3.1. Wind Stress

First, we plot the total wind stress  $\tau$  from the WO experiment derived using the eddy-covariance method (Figure 2). The standard error of wind stress for each condition was found to be  $\mathcal{O}(10^{-2})$  and therefore not shown in Figure 2.  $\tau_{WO}$  follows an approximately quadratic relationship with wind speed and ranges from 0.16 N m<sup>-2</sup> at  $U_{10} = 10.9$  m s<sup>-1</sup> to 18.7 N m<sup>-2</sup> at  $U_{10} = 65.9$  m s<sup>-1</sup>. Then, we normalize  $\tau_{J10}$  and  $\tau_{M7.5}$  with  $\tau_{WO}$  for each wind condition to quantify the change of stress relative in these experiments relative to WO (Figure 3).

The measured stresses from the J10 ( $\tau_{J10}$ ) and M7.5 ( $\tau_{M7.5}$ ) experiments are marginally lower than that of the WO experiment in 10-m winds less than 18 and 31 m s<sup>-1</sup>, respectively.  $\tau_{J10}$  becomes marginally higher than  $\tau_{WO}$  in the  $U_{10}$  range from 31 to 59 m s<sup>-1</sup>, by up to 2%. However,  $\tau_{M7.5}$  is higher than  $\tau_{WO}$ . In both experiments, the relative stress difference peaks at  $U_{10} = 37$  m s<sup>-1</sup>. This increase is more pronounced in steep monochromatic waves (11% maximum increase) than in broad-banded JONSWAP waves (2% maximum increase). This relative difference is important to establish before we proceed to evaluate the sheltering coefficient for each wind and wave condition in Section 3.4.

### 3.3. Wave Spectra

Water surface elevation measured by the capacitance wave wires allows us to compute the wave variance spectra for each wind regime and for each experiment (Figure 5). In the WO experiment, we find a sharp increase and frequency downshift of the wave spectral peak when increasing  $U_{10}$  from 10.9 to 37.2 m s<sup>-1</sup> (Figure 5). However, for stronger winds, the spectral peak exhibits a further downshift of frequency, with no increase in power. One possible mechanism that may explain this regime change is the tearing of wave crests due to direct impact from wind and intensified wave dissipation. This phenomenon has been observed previously in both the field (Holthuijsen



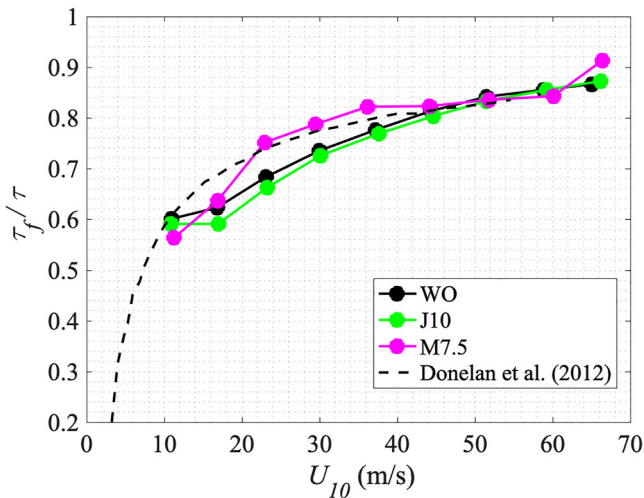


**Figure 4.** Ratio of form stress  $\tau_f$  to total stress  $\tau$  against 10-m wind speed in Wind Only (WO; black), J10 (green), and M7.5 (magenta). Numerical results from Donelan et al. (2012) are plotted in dashed black line.

et al., 2012) and the laboratory (Curcic & Haus, 2020) and is known to occur in hurricane-force winds.

In contrast to the WO experiment, the spectra in J10 maintain their peak at the frequency of 1 Hz, which is the input frequency of the JONSWAP spectrum produced by the wave generator (Figure 5b). This finding supports the results by Lee and Monty (2020) who studied wave growth under wind forcing over background waves with the JONSWAP spectrum and found that the spectral peak of the input waves persists despite the hurricane-force winds. Unlike the WO experiment where the wind-sea peak is evident even in lower wind settings, in the J10 experiment a wind-sea peak does not appear until the wind speeds reach hurricane force. Thus, even the broad-banded mechanically generated waves such as the JONSWAP spectrum are effective at suppressing a significant development of a wind-sea peak. This spectral characteristic is commonly attributed to aerodynamic sheltering of wind sea by longer waves (Chen & Belcher, 2000).

The spectra from the M7.5 experiment are characterized by multiple harmonic peaks at integer multiples of the peak period (Figure 5c). These so-called bound harmonics are an artifact of waves that are not exactly sine-like in form but more peaked being processed with a Fourier transform during the calculation of the spectral density (Donelan et al., 1985). Thus, a Fourier spectrum

of a peaked monochromatic wave results in multiple spectral peaks at integer multiples of the peak period, in our case at 1, 2, 3 s, etc. The bound harmonics are most pronounced in lower wind regimes and become more attenuated with the increase in wind forcing. Unlike the J10 experiment, a secondary wind-sea spectral peak is not evident in the M7.5 experiment in any wind condition. Nevertheless, the high-frequency part of the spectrum increases in energy with the increase in wind speed.

Although the behavior of the wave spectra shown in Figure 5 provides an insight into aerodynamic sheltering in different wind and wave regimes, we will proceed to quantify it more precisely by combining simultaneous and colocated eddy-covariance stress and wave spectrum measurements in the following section.

### 3.4. Quantifying Aerodynamic Sheltering

We first quantify sheltering using following the integrated, frequency-independent sheltering coefficient in Equation 14. Then, we quantify the sheltering as function of wave frequency, following Equation 15. The results of these two approaches are described in the following subsections.

#### 3.4.1. Frequency-Independent Sheltering

Having quantified the total and form stress and wave spectra for all wind and wave regimes, we now proceed to quantify the aerodynamic sheltering following Section 2.4. Figure 6 shows the sheltering coefficient  $A$  as function of 10-m wind speed for all three experiments. All three experiments exhibit an approximately parabolic shape of the sheltering coefficient  $A$  as function of  $U_{10}$  where  $A$  initially decreases and then increases with wind speed. The local minimum of  $A$  is located approximately between  $U_{10}$  of 30 and 35  $\text{m s}^{-1}$ , which corresponds to the transition from tropical storm to Category 1 hurricane-force winds. However, each experiment exhibits a different range of variability of the sheltering coefficient. Specifically,  $A$  falls in the range of 0.07–0.34, 0.05–0.14, and 0.03–0.1 in the case of WO, J10, and M7.5, respectively. Recall that low sheltering coefficient  $A$  indicates higher sheltered area by the long waves. The amount of sheltering thus increases from pure wind sea to broad-banded JONSWAP to steep monochromatic waves.

So far, we have assumed a viscous sublayer where the air flow is laminar and governed by a small Reynolds number (Donelan et al., 2012). By combining Equations 11–13, we computed  $\tau_v$  and thus obtained  $\tau_f$  by subtracting  $\tau_v$  from the measured eddy-covariance stress  $\tau$ . Recall that  $\tau_f$  gradually assumes a dominant role in  $\tau$  in all three experiments (Figure 4). However, this separation of  $\tau_v$  and  $\tau_f$  does not account for the flow separation on the leeward side where the wind streamlines detach from the wave surface and the viscous sublayer is no longer clearly defined. Thus, inaccuracies may arise in our estimation of  $\tau_v$ . To quantify the effect of this

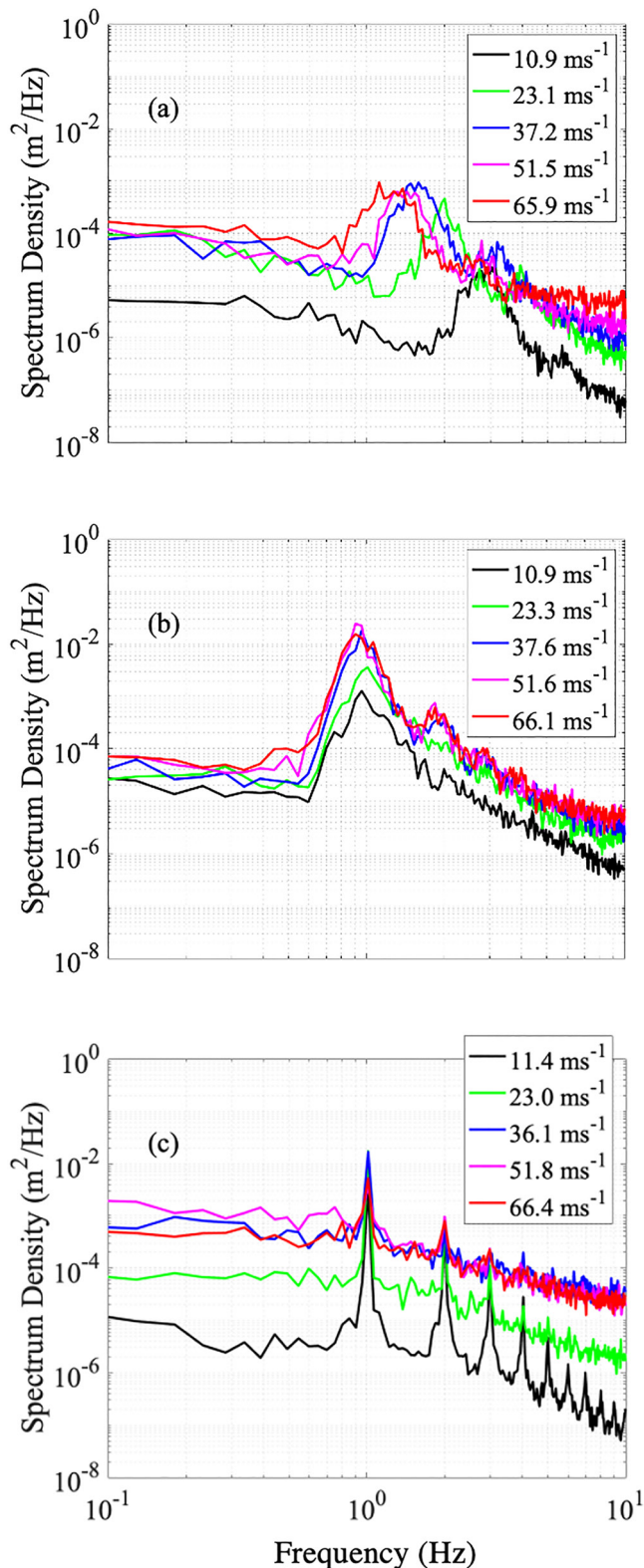


**Figure 5.** Wave variance spectra from experiments (a) Wind Only (WO), (b) J10, and (c) M7.5 under five different wind regimes.

uncertainty on the sheltering coefficient  $A$ , we calculated  $A$  by assuming a  $\pm 25\%$  uncertainty range in the value of  $\tau_v$ . These uncertainties in  $A$  are shown with error bars in Figure 6. The size of these error bars confirms that the sheltering coefficient is not sensitive to the value of  $\tau_v$ , especially in experiments J10 and M7.5. This suggests that the denominator  $D$  in Equation 14 is the dominant contributor to the value of  $A$ . A more accurate estimation of  $\tau_f$  will involve wave-following pressure measurement or a PIV technique (Banner & Peirson, 1998) in the tank, which will be one of the goals of our future research.

To place our sheltering coefficient results in the context of previous studies, we compare them with values obtained from a number of field and laboratory measurements (Donelan & Pierson, 1987; Donelan et al., 2006; Grare, 2009; Mastenbroek et al., 1996; Peirson & Garcia, 2008; Peirson et al., 2014). We plot our estimates of the sheltering coefficient, as well as those from previous studies, against mean wave steepness  $ak$  (Figure 7). A few of these studies considered  $A$  a constant (Donelan, 1999; Donelan & Pierson, 1987; Donelan et al., 2006, 2012). Others (Grare, 2009; Mastenbroek et al., 1996; Peirson & Garcia, 2008; Peirson et al., 2014) obtained  $A$  that varied with  $ak$ . Previous results were derived from pure wind-sea conditions, similar to our WO experiment. However, their wind forcing remained limited to low-to-moderate conditions. Compared to previous work, our results extend the range of  $ak$  beyond the previously measured 0.32 by Peirson et al. (2014), up to the critical steepness of 0.42 in the M7.5 experiment. Our estimates of the sheltering coefficient in pure wind-sea WO are consistent with and in support of the previous work (Grare, 2009; Grare et al., 2013; Mastenbroek et al., 1996). Overall,  $A$  decreases with increasing  $ak$  and asymptotes at values below 0.08 for very steep waves, which is indicative of strong sheltering and possibly flow separation in the lee of these waves.

In summary, the sheltering coefficient  $A$  exhibits significant variability at moderate ( $U_{10} < 20 \text{ m s}^{-1}$ ) and extreme ( $U_{10} > 40 \text{ m s}^{-1}$ ) wind speeds depending on the wave state. Similarly,  $A$  is also highly variable (in the range from 0.05 to 0.35) in wave states of moderate steepness ( $0.12 < ak < 0.25$ ). It is important to better understand the nature and the cause of this variability to allow formulating more accurate wind input source functions for numerical wave models. We explore possible causes of sheltering variability in more depth later in this paper.

### 3.4.2. Frequency-Dependent Sheltering

As the typical wave states in the field are broad banded and often bimodal, a frequency-integrated sheltering coefficient may not be used to characterize the aerodynamic sheltering at different wave scales. Using Equation 17, we evaluate  $A$  as a function of frequency in all three experiments and evaluate it over the shortwave-frequency band of 1–10 Hz (Figure 8). The dominant pattern is that  $A(f)$  decreases with increasing wind forcing across the entire shortwave-frequency band. This implies that higher wind forcing induces more sheltering on shortwaves. Further,  $A(f)$  gradually decreases with frequency. This means that shorter waves are more sheltered than the longer ones. A steep decrease in  $A(f)$  occurs at 1–3 Hz in WO for  $U_{10} = 10.9 \text{ m s}^{-1}$  and at 1–2 Hz for higher wind speeds (Figure 8a). Beyond 3 Hz and  $U_{10} = 23.1 \text{ m s}^{-1}$  (tropical storm-force winds),  $A(f)$  appears to saturate and not decrease any further with increasing winds. This can be explained by the downshifting of the spectral peak in WO that we observed in Figure 5a—as the wind-sea peak shifts to lower frequencies with increasing wind speed,

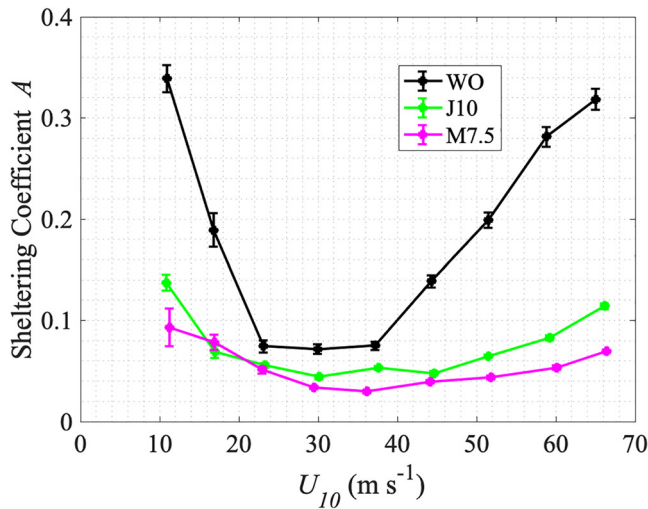


**Figure 6.** Sheltering coefficient  $A$  as function of 10-m wind speed from all three experiments. The error bars show the range of uncertainty in  $A$  resulting if errors in the calculation of  $\tau_v$  are in the range  $\pm 25\%$ .

impact from wind that we observed visually. The absence of  $A(f)$  in this wind regime for waves longer than 2.5 Hz and higher than 9 Hz is due to the negative velocity cospectrum  $\tau(f)$  (i.e., negative or upward momentum flux) in these frequency bands.

### 3.5. Spectral Density and Local Steepness

To better understand the physical mechanism behind the increase of  $A$  with increasing wind speed, we conditionally average the shortwave properties over the phase of a monochromatic long wave. Recall that the sheltering hypothesis proposes that the shortwaves are aerodynamically sheltered by specific geometric features (i.e., crests) of the long wave. Phase-dependent conditional averaging thus allows us to quantify the shortwave properties in relation to the long-wave crests and troughs. First, we obtained the shortwaves' elevation  $\eta_s$  by applying a band-pass filter of 2.1–2.9 Hz over water elevation collected by wave wire. Then, we performed the continuous wavelet transform to obtain the shortwaves' omni-directional wavelet spectrum density  $W_s(\omega, t)$  and calculated shortwaves' local steepness  $\gamma_s$  from  $\eta_s$  mentioned in Section 2.5. An integration of  $W_s(\omega, t)$  on angular frequency  $\omega$  will yield a time series  $W_s(t)$ , in the same dimension as  $\gamma_s$  as well as the water elevation. We then phase-averaged  $\gamma_s$  and  $W_s(t)$  of short-wave over the long-wave phase, using the conditional phase-averaged method mentioned in Section 2.6. To demonstrate how shortwave energy is distributed over the long-wave phase, we normalized omni-directional spectral density  $W_s$  of the shortwave by dividing its mean value over each run time (e.g., Shabani et al., 2022). Thus, the phase-averaged normalized omni-directional spectra represent the shortwave energy distribution over long waves and the local steepness of shortwave represents the geometrical form and breaking intensity of these waves in the M7.5 experiment (Figure 9), with error bars of one standard error.

The normalized spectral density and the local steepness of shortwaves overall have strong dependence on the phase of the long wave (Figure 9). In the lowest wind setting ( $U_{10} = 11.4 \text{ m s}^{-1}$ ), the normalized spectrum of the shortwaves is upwave relative to the long-wave crest and its minimum in its trough (Figure 9a). This is mostly consistent with the traditional hydrodynamic modulation theory based on the dispersion relationship and the conservation of wave crests (Longuet-Higgins & Stewart, 1960) whose

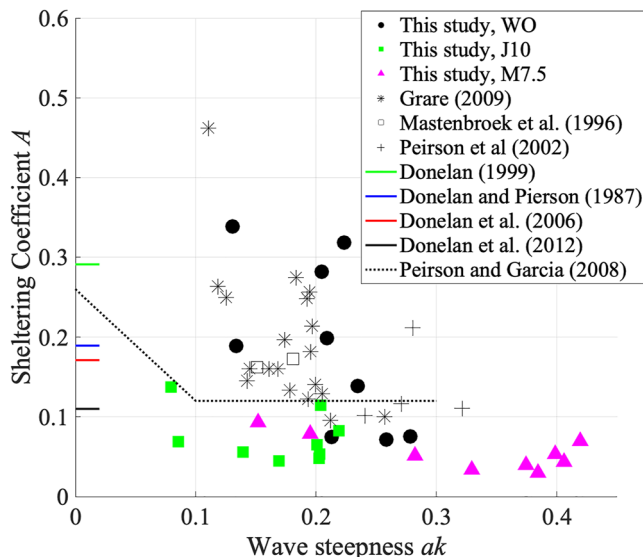


**Figure 7.** Sheltering coefficient  $A$  as a function of mean wave steepness  $ak$ , based on the three experiments in this study, and several previous studies.



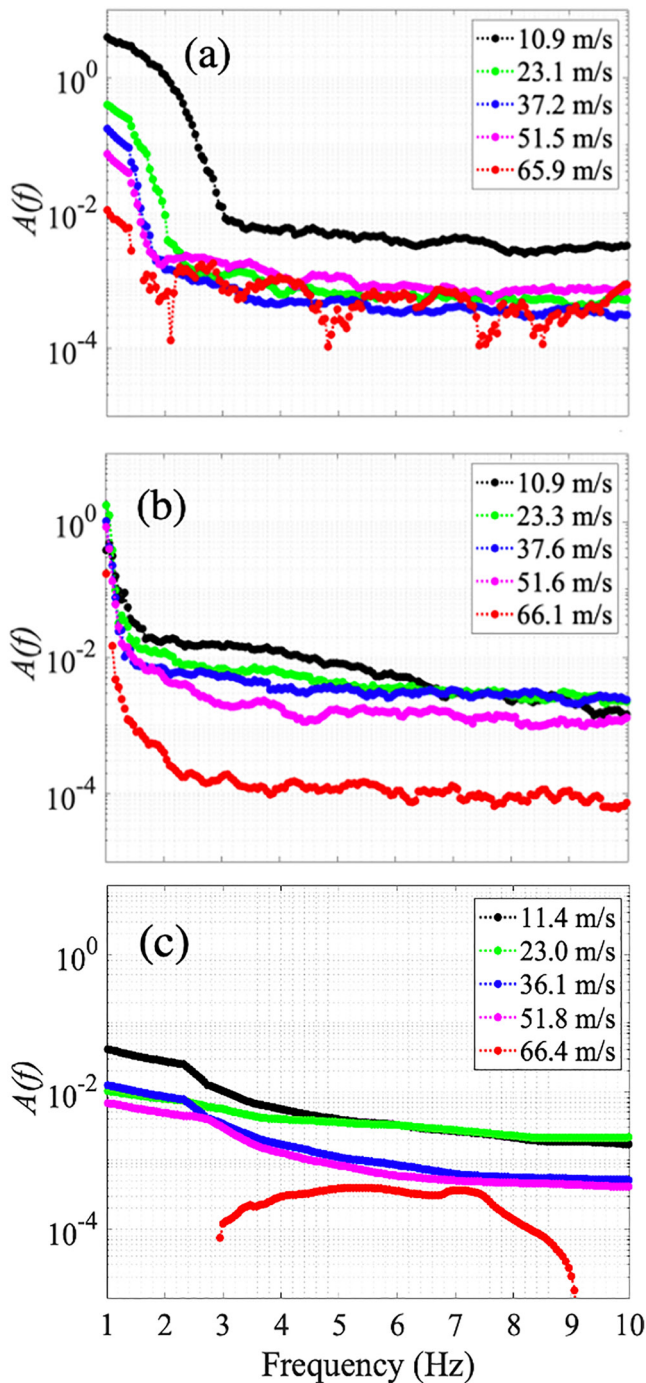


**Figure 8.** Frequency-dependent sheltering coefficient  $A(f)$  from experiments (a) Wind Only (WO), (b) J10, and (c) M7.5 under five different wind regimes.

upward (negative) momentum flux in the swell. While in our laboratory experiments we do not produce swell waves (i.e., waves that out-run the wind), waves that do propagate faster, for example, in experiments J10 and M7.5, are expected to incur lower wind stress overall due to the relative wind terms in Equation 1. However, as  $U_{10}$  increases, wave-induced stress in J10 and M7.5 gradually increases as well and outgrows that of WO. Our

solution finds the highest modulation at the crest. However, as the wind speed increases, the phase of the shortwave spectral peak shifts initially downwave at  $U_{10} = 23.0 \text{ m s}^{-1}$  and then upwave again for higher wind speeds, consistent with the findings by Donelan et al. (2010). The downwave location of the peak at  $U_{10} = 23.0 \text{ m s}^{-1}$  may be associated with the whitecapping of the long wave on its front face, which transfers some of the long-wave energy to higher frequencies. This result can be attributed to two distinct processes: First, the wind forcing on the rear face of the long wave generates shortwaves and results in the increase of their spectral density; second, the front face of the steep long wave amplifies the breaking of the shortwave by increasing their steepness (Donelan et al., 2012). The range of error bars for  $W_s$  has the nondimensional scale of 0.04 and is not phase dependent. Thus, we consider the distribution of  $W_s$  along long-wave's phase as statistically representative.

In contrast to the normalized spectral density, the local steepness  $\gamma_s$  of the shortwaves exhibits two local maxima and minima each over the phase of the long wave (Figure 9b). The range of error bars for  $\gamma_s$  is relatively small compared to those of  $W_s$  and is barely visible until wind forcing reaches  $66.4 \text{ m s}^{-1}$  on the windward side. Thus, we also consider  $\gamma_s$  distribution along long-wave's phase as statistically representative. The first peak occurs on the windward side ( $0^\circ$ – $180^\circ$ ) and the second peak on the leeward side ( $180^\circ$ – $360^\circ$ ). The peak on the windward side is larger than that at leeward side in all wind regimes. Like the spectral density, the local steepness peak on the windward face of the long wave also shifts upwind with increasing wind speed. Once  $U_{10}$  exceeds  $36.1 \text{ m s}^{-1}$ , the peak of  $\gamma_s$  exceeds the breaking threshold 0.6 (Liu & Babanin, 2004). In such circumstance, shortwaves have a high probability of breaking.  $\gamma_s$  peaks also do not occur in the same long-wave phase as  $W_s$  peak in (a). Such discrepancy is particularly observable after wind once exceeds in the same  $\text{m s}^{-1}$  where windward  $\gamma_s$  peak exceeds the breaking threshold. Thus, in hurricane-force winds, although  $\gamma_s$  reach a maximum, the strongest energy occurred at a different long-wave phase due to the intense breaking at the  $\gamma_s$  peak. A similar phenomenon was observed by Donelan et al. (2010) who found that as the wavenumber moves above the spectral peak, the long waves modulate the shortwave spectral density and drive it into a breaking-limited saturation state. Thus, we interpret this disparity between  $\gamma_s$  and  $W_s$  to be the result of shortwave breaking due to both hydrodynamic and aerodynamic modulation (the sheltering effect, which is observed from the value of sheltering coefficient and the phase variability of  $\gamma_s$ 's peak on the long wave). Meanwhile, the leeward  $\gamma_s$  peak remains under the breaking threshold without a significant phase shift. We suspect that this may be due to a combination of increasing hydrodynamic modulation and decreasing aerodynamic modulation on the forward face of the long wave. However, further research (ideally using PIV techniques) is needed to verify such assumption.

## 4. Discussion

### 4.1. Wind Stress Variability

Vincent et al. (2019) found based on field measurements that swell modulates the wind stress. In their study,  $U_{10}$  did not exceed  $20 \text{ m s}^{-1}$  and they found an

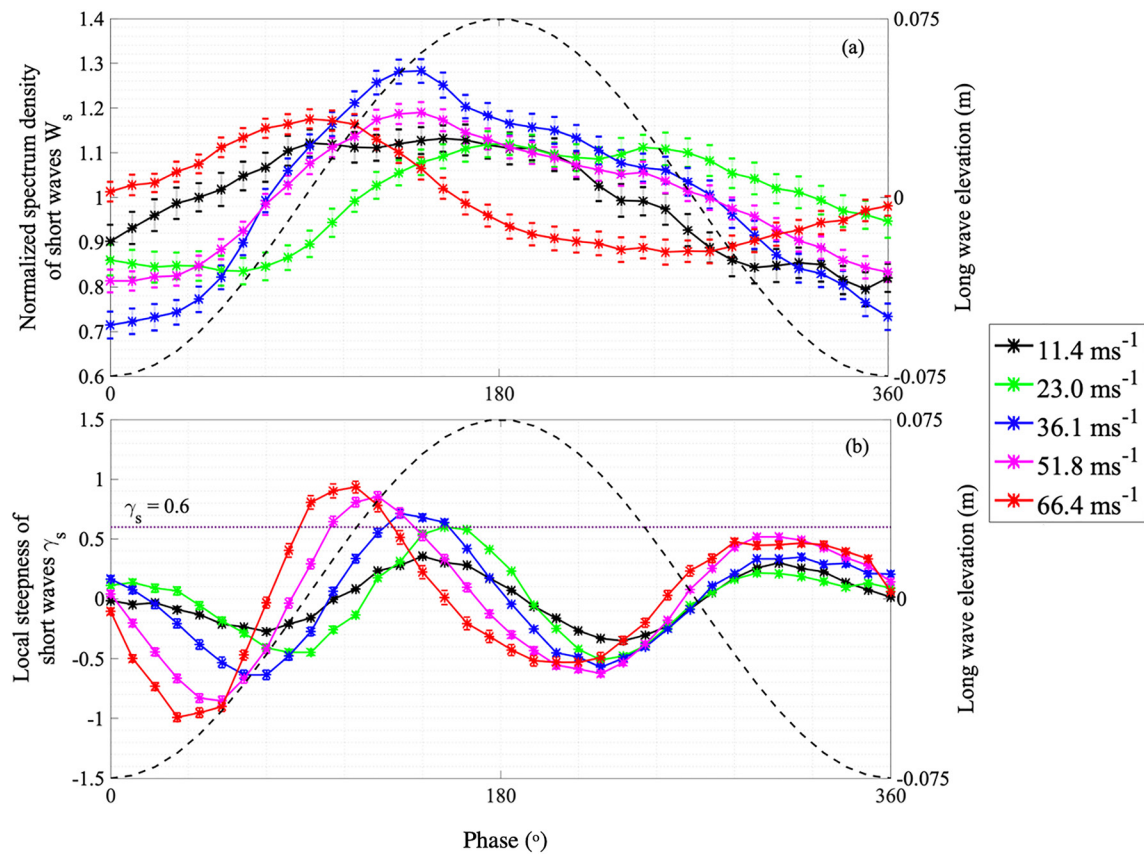


**Figure 9.** Conditional phase average of (a) normalized omni-directional short wind-wave spectral density and (b) short wind-wave local steepness  $\gamma_s$  over long-wave phase under different wind speed from M7.5. Y-axis on the right represents the long-wave's elevation, where the long wave is shown by black dashed line. The black dotted line ( $\gamma = 0.6$ ) is the threshold used to identify breaking by Liu and Babanin (2004). The error bar is defined as the range of one standard error within each phase bin.

visual observation of whitecapping and frequent breaking at wave crests confirms frequent breaking of peak waves in the same forcing range ( $U_{10} > 30 \text{ m s}^{-1}$ ). Further, Babanin et al. (2007) discussed the variability of  $\tau$  with breaking events. Their results showed that following wave breaking there is an increase in wind input, which is primarily manifested as the pressure difference between the windward and leeward faces of the wave. They concluded that breaking events increase wind stress  $\tau$ .

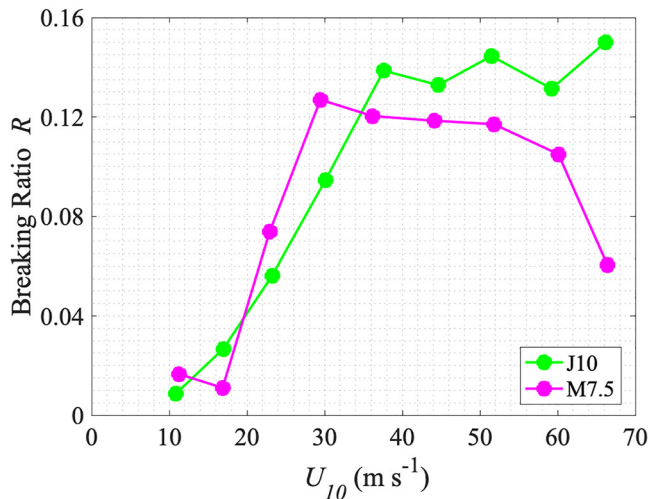


**Figure 10.** Breaking ratio  $R$  in J10 (green) and M7.5 for each wind forcing.

To better understand the cause of the wind stress variability between different J10 and M7.5 experiments, we first isolate the water elevation associated with the mechanically generated waves by applying a band-pass filter (the filter ranges from 0.8 to 1.2 Hz). Then, we calculate the local steepness of the mechanically generated waves  $\gamma$  as described in Section 2.5. Since local steepness is an indicator of breaking events, its value yields information about the breaking of the long waves (Liu & Babanin, 2004). Then, we relate the wave breaking to the  $\tau$  variability by defining the breaking ratio  $R$  as the ratio of long waves with  $\gamma > 0.6$  to all long waves, following Liu and Babanin (2004). This is shown in Figure 10. J10 and M7.5 show a similar trend of breaking ratio suddenly increasing with wind speed from 16  $\text{m s}^{-1}$  wind speeds to approximately 30  $\text{m s}^{-1}$  wind speeds. In hurricane-force winds, the breaking ratio saturates at approximately 0.14 and 0.12 in experiments J10 and M7.5, respectively. Unlike that of the J10 experiment, the breaking ratio in the M7.5 experiment exhibits a decrease in extreme winds ( $U_{10} > 50 \text{ m s}^{-1}$ ). This decrease may be caused by the intense wave dissipation due to direct impact from wind, which we can visually observe to



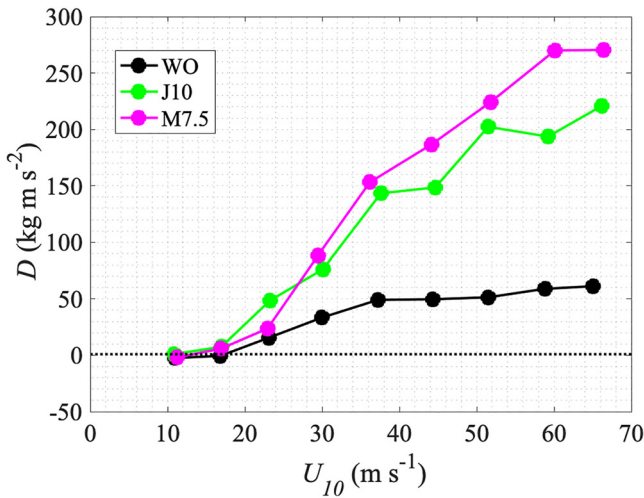


**Figure 11.** Sheltering coefficient denominator  $D$  from all experiments as function of 10-m wind speed.

After  $U_{10}$  exceeds 20 m s<sup>-1</sup>, strong breaking (large  $R$ , Figure 10) and wave energy saturation occur, as seen in the spectral peaks that did not further increase with wind speed (Figure 5). The breaking of high waves increases the sheltered area and reduces the sheltering coefficient.

It may provide further insight into the sheltering of shorter waves to integrate Equation 16 over the frequency band of 1–10 Hz:

$$A_{in} = \int_{1\text{Hz}}^{10\text{Hz}} A(f) df \quad (22)$$

We compare shortwave-banded  $A_{in}$  to the total integrated sheltering coefficient in  $A$  for all experiments and wind conditions (Figure 12). Unlike  $A$  which has an overall parabolic shape in all three experiments,  $A_{in}$  exhibits an overall decrease with wind speed. The shortwaves in the 1–10 Hz frequency band become increasingly more sheltered with increasing wind speed.  $A_{in}$  under  $U_{10}$  of 10.9 m s<sup>-1</sup> in WO is exceptionally large (2.7, not shown in Figure 12a) compared to other  $A_{in}$  values under stronger wind forcings in WO. This is because of the absence of paddle waves and lowest wind forcing, which rendered relatively weak sheltering effect on shorter waves and henceforth, a large  $A_{in}$  value. In the WO and J10 experiments,  $A_{in}$  is larger than their respective  $A$  in  $U_{10} < 30$  m s<sup>-1</sup> and  $U_{10} < 50$  m s<sup>-1</sup>, respectively. However, under extreme wind forcing,  $A_{in}$  becomes smaller than  $A$ . Unlike in J10 and WO,  $A_{in}$  in M7.5 is smaller than  $A$  in all wind conditions. This is because the M7.5 experiment has the dominant wave that is steep and monochromatic, which effectively sheltered all shorter waves.

#### 4.3. Side-Camera Imaging of Wave Growth and Breaking

With the aid of a side-mounted digital camera with sampling frequency at 20 Hz, we visualized the air–sea interface on the windward and leeward faces of each passing wave with increasing wind speeds (Figure 13). We select photographs that were illustrative of the typical process of wind forcing and wave breaking during the M7.5 experiment. The images are of the windward and leeward faces of the same monochromatic wave.

Under  $U_{10}$  values of 10.9 m s<sup>-1</sup>, windward and leeward faces appear smooth and maintain a nearly sine-like shape. An increase in amplitude can be seen on windward face under  $U_{10}$  of 23.1 m s<sup>-1</sup> due to wind input (Figure 13c). As wind forcing increased, shorter waves become more prominent on the windward face (Figures 13e and 13g). This is consistent with our local steepness results from Figure 9 where we found a local maximum of shortwave steepness on the windward face of the long wave. On the leeward face of the wave and beginning with  $U_{10}$  of 36.1 m s<sup>-1</sup>, we see evidence of intense, plunging wave breaking, with bubbles, spume, and spray generation (Figures 13f, 13h, and 13j). Finally, in the most extreme wind condition, the windward face of the wave shows evidence of the wave tearing and spume generation due to direct impact from wind on the wave crest (Figure 13i).

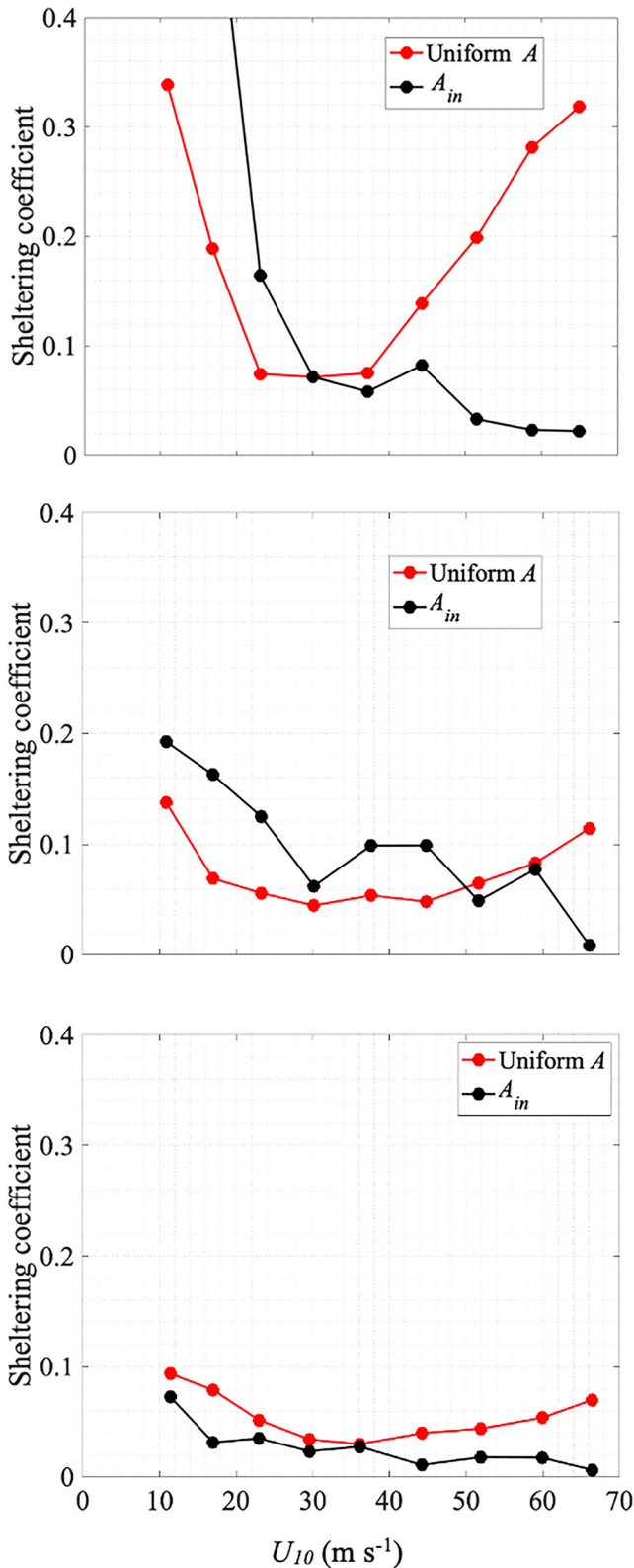


**Figure 12.** Shortwave-banded sheltering coefficient  $A_{in}$  and total integrated sheltering coefficient  $A$  from experiments (a) Wind Only (WO), (b) J10, and (c) M7.5 in different wind conditions.

The side-mounted camera images of growing and breaking waves thus provide visual support of some of our results and interpretations presented in the previous sections.

## 5. Conclusions

In this study, we quantified the aerodynamic sheltering of shortwaves by longer waves using the JS hypothesis and high-frequency laboratory measurements of waves and stress in a wide range of wave states and wind conditions. We conclude with several takeaways:

1. We find that the sheltering coefficient is not constant, as was previously commonly assumed. Instead, the sheltering coefficient varies significantly depending on the wave state and the wind forcing.
2. The sheltering coefficient is an approximately parabolic function of wind speed: it first decreases with wind speed up to  $U_{10} \approx 30 \text{ m s}^{-1}$  (corresponding to the transition from tropical storm-force to hurricane-force winds) where it saturates with the value between 0.04 and 0.08; then, it increases with wind speed, reaching values between 0.08 and 0.32, depending on the background wave state.
3. The sheltering coefficient also varies greatly with the background wave state. Pure wind-sea yields higher sheltering coefficients (0.08–0.32), while a broad-banded JONSWAP spectra and monochromatic waves yield significantly lower sheltering coefficients with ranges of 0.05–0.14 and 0.04–0.09, respectively. Overall, steeper and more narrow-banded waves yield stronger sheltering (but lower sheltering coefficient) of the shortwaves.
4. Our estimates of the sheltering coefficient complement the existing, albeit scarce, data sets from previous studies (Grare et al., 2013), and extend the ranges of previously studied conditions both in terms of wind speed and wave steepness.
5. Phase-dependent bin-averaging over many consecutive phases of the monochromatic long wave reveals an overall downshift of shortwave spectra and a gradual increase of the shortwave steepness on the windward face of the long wave with increasing wind speed.
6. Side-camera imaging provides visual evidence of the development of short, steep waves on the windward face of the long wave due to strong wind forcing. As the winds become extreme (major hurricane force), intense wave breaking and tearing of wave crests due to direct impact from wind is evident.
7. More detailed measurements, especially using PIV techniques on the air-side of the wavy interface, are needed to provide a more in-depth understanding of aerodynamic sheltering of shortwaves in extreme winds. This is important because the wind input functions in the current spectral wave models do not resolve this physical process to a sufficient detail.
8. Our results stress the need for a more accurate and comprehensive parameterization of aerodynamic sheltering that takes into account not only the wind speed but also the shape and amplitude of the wave spectrum. Our future work will attempt to fill this gap while building on top of results presented here.

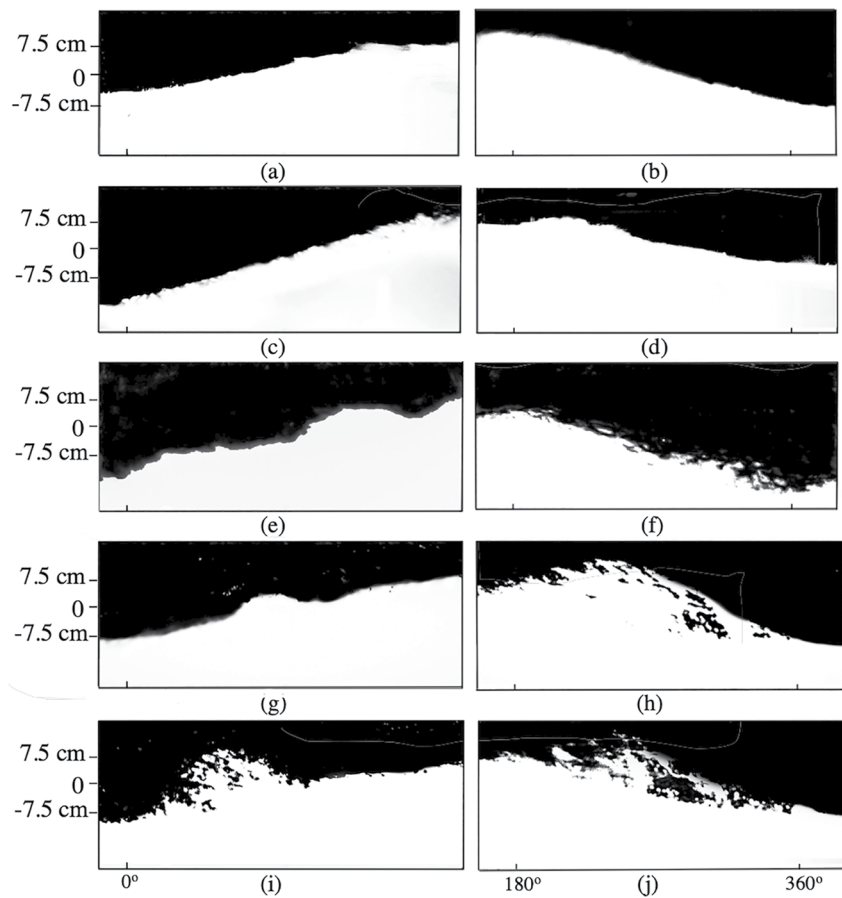


**Figure 13.** Photographs of waves during the M7.5 experiment of the windward (a, c, e, g, and i) and leeward (b, d, f, h, and j) faces and  $U_{10}$  values of  $11.4 \text{ m s}^{-1}$  (a, b),  $23.0 \text{ m s}^{-1}$  (c, d),  $36.1 \text{ m s}^{-1}$  (e, f),  $51.8 \text{ m s}^{-1}$  (g, h), and  $66.4 \text{ m s}^{-1}$  (i, j). The contrast was enhanced and image cropped to isolate and center on the air–water interface. The waves are propagating from left to right.

## Data Availability Statement

The quality-controlled data used in this paper can be found at: <https://zenodo.org/record/7764266>.

## Acknowledgments

We thank Cedric Guigand, Mohammad Ghiasian, Kathrine Devore, and Luke Arends for their help with setting up the laboratory experiments. We thank William Drennan and Nathan Laxague for reviewing early versions of this manuscript and for providing valuable feedback. We also thank anonymous reviewers for their help with improving this manuscript. This study was supported by the National Science Foundation Award 1745384. We also thank the FACE Foundation and the Thomas Jefferson Fund for funding the publication fees for this paper. The data from our experiments are provided in Supporting Information S1.

## References

- Babani, A. V., Banner, M. L., Young, I. R., & Donelan, M. A. (2007). Wave-follower field measurements of the wind-input spectral function. Part III: Parameterization of the wind-input enhancement due to wave breaking. *Journal of Physical Oceanography*, 37(11), 2764–2775. <https://doi.org/10.1175/2007JPO3757.1>
- Banner, M. L., & Peirson, W. (1998). Tangential stress beneath wind-driven air–water interfaces. *Journal of Fluid Mechanics*, 364, 115–145. <https://doi.org/10.1017/S0022112098001128>
- Buckley, M. P., & Veron, F. (2016). Structure of the airflow above surface waves. *Journal of Physical Oceanography*, 46(5), 1377–1397. <https://doi.org/10.1175/JPO-D-15-0135.1>
- Buckley, M. P., & Veron, F. (2019). The turbulent airflow over wind generated surface waves. *European Journal of Mechanics B: Fluids*, 73, 132–143. <https://doi.org/10.1016/j.euromechflu.2018.04.003>
- Chen, G., & Belcher, S. E. (2000). Effects of long waves on wind-generated waves. *Journal of Physical Oceanography*, 30(9), 2246–2256. [https://doi.org/10.1175/1520-0485\(2000\)030<2246:EOLWOW>2.0.CO;2](https://doi.org/10.1175/1520-0485(2000)030<2246:EOLWOW>2.0.CO;2)
- Curcic, M., & Haus, B. K. (2020). Revised estimates of ocean surface drag in strong wind. *Geophysical Research Letters*, 47, e2020GL087647. <https://doi.org/10.1029/2020GL087647>
- Donelan, M. A. (1999). In S. G. Sajjadi, N. H. Thomas, & J. C. R. Hunt (Eds.), *Wind-induced growth and attenuation of laboratory waves in wind-over-wave couplings: Perspectives and prospects*. Oxford University Press.
- Donelan, M. A., Babani, A. V., Young, I. R., & Banner, M. L. (2006). Wave-follower field measurements of the wind-input spectral function. Part II: Parameterization of the wind input. *Journal of Physical Oceanography*, 36(8), 1672–1689. <https://doi.org/10.1175/JPO2933.1>
- Donelan, M. A., Curcic, M., Chen, S. S., & Magnusson, A. K. (2012). Modeling waves and wind stress. *Journal of Geophysical Research*, 117, C00J23. <https://doi.org/10.1029/2011JC007787>

- Donelan, M. A., Hamilton, J., & Hui, W. H. (1985). Directional spectra of wind-generated ocean waves. *Philosophical Transactions of the Royal Society of London, Series A: Mathematical and Physical Sciences*, 315(1534), 509–562. <https://doi.org/10.1098/rsta.1985.0054>
- Donelan, M. A., Haus, B. K., Plant, W. J., & Troianowski, O. (2010). Modulation of short wind waves by long waves. *Journal of Geophysical Research*, 115, C10003. <https://doi.org/10.1029/2009JC005794>
- Donelan, M. A., Haus, B. K., Reul, N., Plant, W. J., Stiassnie, M., Graber, H. C., & Saltzman, E. S. (2004). On the limiting aerodynamic roughness of the ocean in very strong winds. *Geophysical Research Letters*, 31, L18306. <https://doi.org/10.1029/2004GL019460>
- Donelan, M. A., & Pierson, W. J., Jr. (1987). Radar scattering and equilibrium ranges in wind-generated waves with application to scatterometry. *Journal of Geophysical Research*, 92(C5), 4971–5029. <https://doi.org/10.1029/JC092iC05p04971>
- Donelan, M. A., & Plant, W. J. (2009). A threshold for wind-wave growth. *Journal of Geophysical Research*, 114, C07012. <https://doi.org/10.1029/2008JC005238>
- Drennan, W., Kahma, K., & Donelan, M. (1999). On momentum flux and velocity spectra over waves. *Boundary-Layer Meteorology*, 92(3), 489–515. <https://doi.org/10.1023/A:1002054820455>
- Edson, J. B., Hinton, A. A., Prada, K. E., Hare, J. E., & Fairall, C. W. (1998). Direct covariance flux estimates from mobile platforms at sea. *Journal of Atmospheric and Oceanic Technology*, 15(2), 547–562. [https://doi.org/10.1175/1520-0426\(1998\)015<0547:DCFEFM>2.0.CO;2](https://doi.org/10.1175/1520-0426(1998)015<0547:DCFEFM>2.0.CO;2)
- Grare, L. (2009). *Étude des interactions océan-atmosphère à proximité immédiate de l'interface: Application aux vagues de vent et aux vagues extrêmes* (unpublished doctoral dissertation). Université de la Méditerranée-Aix-Marseille II.
- Grare, L., Peirson, W., Branger, H., Walker, J. W., Giovanangeli, J. P., & Makin, V. (2013). Growth and dissipation of wind-forced, deep-water waves. *Journal of Fluid Mechanics*, 722, 5–50. <https://doi.org/10.1017/jfm.2013.88>
- Hasselmann, K., Barnett, T., Bouws, E., Carlson, H., Cartwright, D., Enke, K., et al. (1973). Measurements of wind-wave growth and swell decay during the Joint North Sea Wave Project (JONSWAP). *Deutsches Hydrographisches Institut*, 8, 1–95.
- Holthuijsen, L. H., Powell, M. D., & Pietrzak, J. D. (2012). Wind and waves in extreme hurricanes. *Journal of Geophysical Research*, 117, C09003. <https://doi.org/10.1029/2012JC007983>
- Hristov, T. (2018). Mechanistic, empirical and numerical perspectives on wind-waves interaction. *Procedia IUTAM*, 26, 102–111. <https://doi.org/10.1016/j.piutam.2018.03.010>
- Husain, N. T., Hara, T., Buckley, M. P., Yousefi, K., Veron, F., & Sullivan, P. P. (2019). Boundary layer turbulence over surface waves in a strongly forced condition: LES and observation. *Journal of Physical Oceanography*, 49(8), 1997–2015. <https://doi.org/10.1175/JPO-D-19-0070.1>
- Husain, N. T., Hara, T., & Sullivan, P. P. (2022). Wind turbulence over misaligned surface waves and air–sea momentum flux. Part I: Waves following and opposing wind. *Journal of Physical Oceanography*, 52(1), 119–139. <https://doi.org/10.1175/jpo-d-21-0043.1>
- Jeffreys, H. (1924). On the formation of waves by wind. *Proceedings of the Royal Society*, 107A, 189–206. <https://doi.org/10.1098/rspa.1925.0015>
- Jeffreys, H. (1925). On the formation of waves by wind. II. *Proceedings of the Royal Society*, 110A, 241–247. <https://doi.org/10.1098/rspa.1926.0014>
- Jones, I., & Toba, Y. (2001). *Wind stress over the ocean*. Cambridge University Press. <https://doi.org/10.1017/CBO9780511552076>
- Laxague, N. J., Curcic, M., Björkvist, J.-V., & Haus, B. K. (2017). Gravity-capillary wave spectral modulation by gravity waves. *IEEE Transactions on Geoscience and Remote Sensing*, 55(5), 2477–2485. <https://doi.org/10.1109/tgrs.2016.2645539>
- Lee, J. H., & Monty, J. P. (2020). On the interaction between wind stress and waves: Wave growth and statistical properties of large waves. *Journal of Physical Oceanography*, 50(2), 383–397. <https://doi.org/10.1175/JPO-D-19-0112.1>
- Li, T., & Shen, L. (2022). The principal stage in wind-wave generation. *Journal of Fluid Mechanics*, 934, A41. <https://doi.org/10.1017/jfm.2021.1153>
- Liu, P. C., & Babanin, A. V. (2004). Using wavelet spectrum analysis to resolve breaking events in the wind wave time series. *Annales Geophysicae*, 22(10), 3335–3345. <https://doi.org/10.5194/angeo-22-3335-2004>
- Longuet-Higgins, M., & Stewart, R. (1960). Changes in the form of short gravity waves on long waves and tidal currents. *Journal of Fluid Mechanics*, 8(4), 565–583. <https://doi.org/10.1017/S0022112060000803>
- Makin, V., Kudryavtsev, V., & Mastenbroek, C. (1995). Drag of the sea surface. *Boundary-Layer Meteorology*, 73(1), 159–182. <https://doi.org/10.1007/BF00708935>
- Mastenbroek, C., Makin, V., Garat, M., & Giovanangeli, J.-P. (1996). Experimental evidence of the rapid distortion of turbulence in the air flow over water waves. *Journal of Fluid Mechanics*, 318(-1), 273–302. <https://doi.org/10.1017/S0022112096007124>
- Miles, J. W. (1959). On the generation of surface waves by shear flows. Part 2. *Journal of Fluid Mechanics*, 6(4), 568–582. <https://doi.org/10.1017/S0022112059000830>
- Monin, A., & Yaglom, A. M. (1971). *Statistical fluid mechanics, volumes 1 and 2*. MIT Press.
- Montalvo, P., Kraenkel, R., Manna, M. A., & Kharif, C. (2013). Wind-wave amplification mechanisms: Possible models for steep wave events in finite depth. *Natural Hazards and Earth System Sciences*, 13(11), 2805–2813. <https://doi.org/10.5194/nhess-13-2805-2013>
- Peirson, W., & Garcia, A. W. (2008). On the wind-induced growth of slow water waves of finite steepness. *Journal of Fluid Mechanics*, 608, 243–274. <https://doi.org/10.1017/S002211200800205X>
- Peirson, W., Walker, J., & Banner, M. (2014). On the microphysical behaviour of wind-forced water surfaces and consequent re-aeration. *Journal of Fluid Mechanics*, 743, 399–447. <https://doi.org/10.1017/jfm.2013.681>
- Phillips, O. M. (1957). On the generation of waves by turbulent wind. *Journal of Fluid Mechanics*, 2(5), 417–445. <https://doi.org/10.1017/S0022112057000233>
- Riley, D. S., Donelan, M. A., & Hui, W. (1982). An extended Miles' theory for wave generation by wind. *Boundary-Layer Meteorology*, 22(2), 209–225. <https://doi.org/10.1007/BF00118254>
- Savelyev, I. B., Haus, B. K., & Donelan, M. A. (2011). Experimental study on wind-wave momentum flux in strongly forced conditions. *Journal of Physical Oceanography*, 41(7), 1328–1344. <https://doi.org/10.1175/2011JPO4577.1>
- Shabani, B., Ware, P., & Baldock, T. E. (2022). Suppression of wind waves in the presence of swell: A physical modeling study. *Journal of Geophysical Research: Oceans*, 127, e2021JC018306. <https://doi.org/10.1029/2021JC018306>
- Stewart, R. W. (1967). Mechanics of the air–sea interface. *The Physics of Fluids*, 10(9), S47–S55. <https://doi.org/10.1063/1.1762504>
- Takagaki, N., Komori, S., Suzuki, N., Iwano, K., Kuramoto, T., Shimada, S., et al. (2012). Strong correlation between the drag coefficient and the shape of the wind sea spectrum over a broad range of wind speeds. *Geophysical Research Letters*, 39, L23604. <https://doi.org/10.1029/2012GL053988>
- Tennekes, H., & Lumley, J. L. (1972). *A first course in turbulence*. MIT Press.
- Touboul, J., Kharif, C., Pelinovsky, E., & Giovanangeli, J. P. (2008). On the interaction of wind and steep gravity wave groups using Miles' and Jeffreys' mechanisms. *Nonlinear Processes in Geophysics*, 15(6), 1023–1031. <https://doi.org/10.5194/npg-15-1023-2008>
- Uz, B. M., Donelan, M. A., Hara, T., & Bock, E. J. (2002). Laboratory studies of wind stress over surface waves. *Boundary-Layer Meteorology*, 102(2), 301–331. <https://doi.org/10.1023/A:1013119313063>

- Vincent, C. L., Thomson, J., Graber, H. C., & Collins, C. O. (2019). Impact of swell on the wind-sea and resulting modulation of stress. *Progress in Oceanography*, 178, 102164. <https://doi.org/10.1016/j.pocan.2019.102164>
- Wright, C. W., Walsh, E. J., Vandemark, D., Krabill, W. B., Garcia, A. W., Houston, S. H., et al. (2001). Hurricane directional wave spectrum spatial variation in the open ocean. *Journal of Physical Oceanography*, 31(8), 2472–2488. [https://doi.org/10.1175/1520-0485\(2001\)031<2472:HDWSSV>2.0.CO;2](https://doi.org/10.1175/1520-0485(2001)031<2472:HDWSSV>2.0.CO;2)
- Yang, D., Meneveau, C., & Shen, L. (2013). Dynamic modelling of sea-surface roughness for large-eddy simulation of wind over ocean wavefield. *Journal of Fluid Mechanics*, 726, 62–99. <https://doi.org/10.1017/jfm.2013.215>